Aseismic strain localization prior to failure and associated seismicity in crystalline rock: Supplementary Material

1 Material properties of Rotondo granite

In this study, Rotondo granite sourced from the Bedretto Underground Laboratory for Geosciences and Geoenergies (BULGG) was used. Rotondo granite is part of the Gotthard massif, and two types can be distinguished along BULGG: equigranular and porphyritic (Rast, 2020). The samples tested in this research were extracted from the tunnel meter 2043 and identified as the equigranular type (Rast, 2020). Figure 1 shows photomicrographs of thin sections of the equigranular Rotondo granite. The quartz occurs in three varieties with an average grain size of 0.35 mm. Alkali feldspar in the granite forms grains in the millimeter range, typically anhedral in shape. Biotite crystals, approximately 1 mm wide, are present as subhedral to anhedral grains (Hafner, 1958; Steck, 1976; Labhart, 2005; Rast, 2020). Based on this description, we estimate the average grain size of $\sim$ 1mm for the equigranular Rotondo granite.

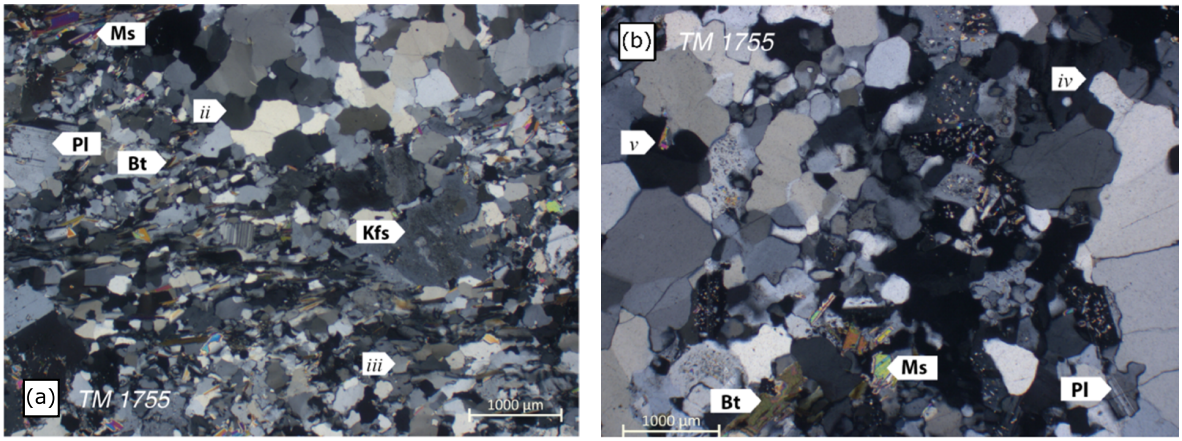

Figure 1 Adapted from Rast (2020). (a) and (b) Thin sections of the equigranular Rotondo granite used in this work. The granite has a main mineral content of quartz (*ii* and *iii*; 25-35%), alkali feldspar (Kfs; 20-40%), plagioclase (Pl; 10-25%) and biotite (Bt; 3-8%); Additionally, garnet, phengite, chlorite, epidote, apatite, muscovite (Ms), zircon and opaques are present as accessory minerals (Hafner, 1958; Steck, 1976; Labhart, 2005; Rast, 2020). (*iv*) irregular grain boundary, (*v*) pinning structure (Rast, 2020).

Table 1 gives a summary of the mechanical properties of Rotondo granite taken from the comprehensive study of David et al (2020).

Table 1 Properties of the Rotondo granite in dry and unconfined conditions (David et al, 2020).

Property	Specification (unit)	Value
Density	ρ (kg/m^3)	2606
Porosity	ϕ (%)	1.75 ± 0.11
P-wave velocity	V_p (m/s)	3501 ± 301 (4000)
S-wave velocity	V_s (m/s)	1785 ± 117
Dynamic Young's modulus	E_{dyn} (GPa)	22.6 ± 2.7
Dynamic Poisson's ratio	ν_{dyn} (-)	0.36 ± 0.03
Young's modulus	E (GPa)	51.5± 1*
Poisson's ratio	ν (GPa)	0.31± 0.05*
Compressive strength	σ_p (MPa)	172 (300±50*)
Tensile strength	σ_t (MPa)	8
Fracture toughness	Mode I (MPa m$^{1/2}$)	1.3
	Mode II (MPa m$^{1/2}$)	4

*Properties measured at a confining pressure of 10 MPa

2 Mechanical response of Rotondo granite

The mechanical response of the Rotondo granite is shown in Figure 2. The AE events are represented using the blue circles, while diamonds indicate the P-wave velocity measured at four heights of the sample. The right panel shows a zoom to the last relaxation phase.

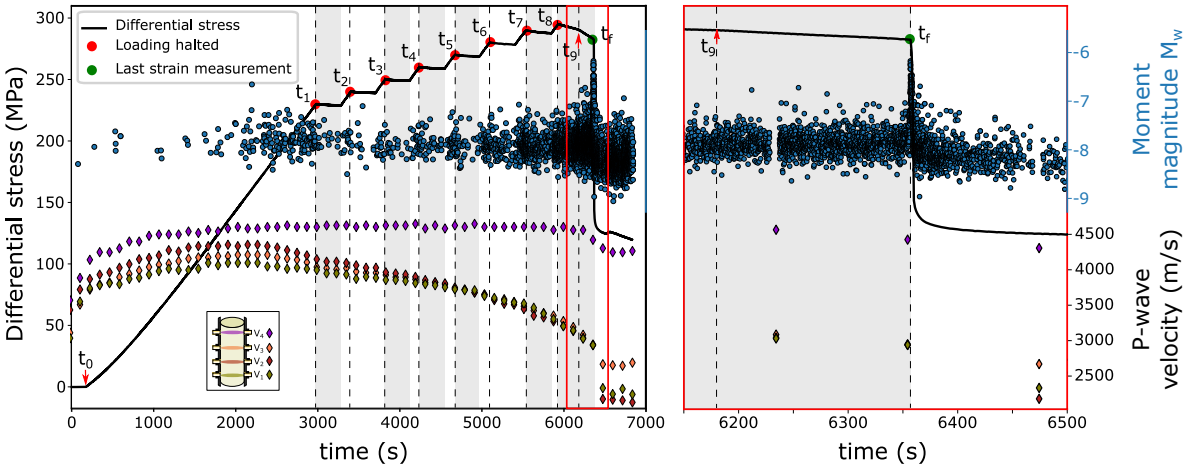

Figure 2 Mechanical response of the Rotondo granite, temporal evolution of AE magnitudes (blue circles) and P-wave velocity during the test. The time interval marked by the light red box (6150 s - 6500 s) is zoomed on the right panel.

3 AE source type

Figure 3 shows the Hudson plot representation of the moment tensor solution (Hudson et al, 1989), computed from the AEs. The seismic events are predominantly distributed in a band oriented in the positive and negative linear dipole direction (LVD(+) and LVD(-), respectively). The events producing an LVD(+) signature also exhibited the highest recorded moment magnitudes, suggesting that a fault type characterized by shear-opening mechanisms was nucleating towards failure. This combination of source type and high moment magnitude (M_w) has been observed in similar triaxial experiments, where shear fractures were induced in sandstone (Kwiatek et al, 2014). In a similar study, Dong et al (2020) observed AEs with higher isotropic components (i.e., explosion and implosion) in a saturated granite sample tested under uniaxial conditions. This difference could be attributed to the higher confinement used in the present work.

Feignier and Young (1992) introduced the R value to quantify the source mechanism of AE events. This parameter represents the ratio of the isotropic component to the sum of the isotropic and deviatoric components. They suggested that a minimum of 30% of isotropic component ($R > 30\%$) is required to generate statistically significant differences between isotropic and deviatoric mechanisms. In our experiment, 97% of the events had an isotropic component below this threshold, confirming the dominance of deviatoric AE events (or "shear" events; Feignier and Young, 1992).

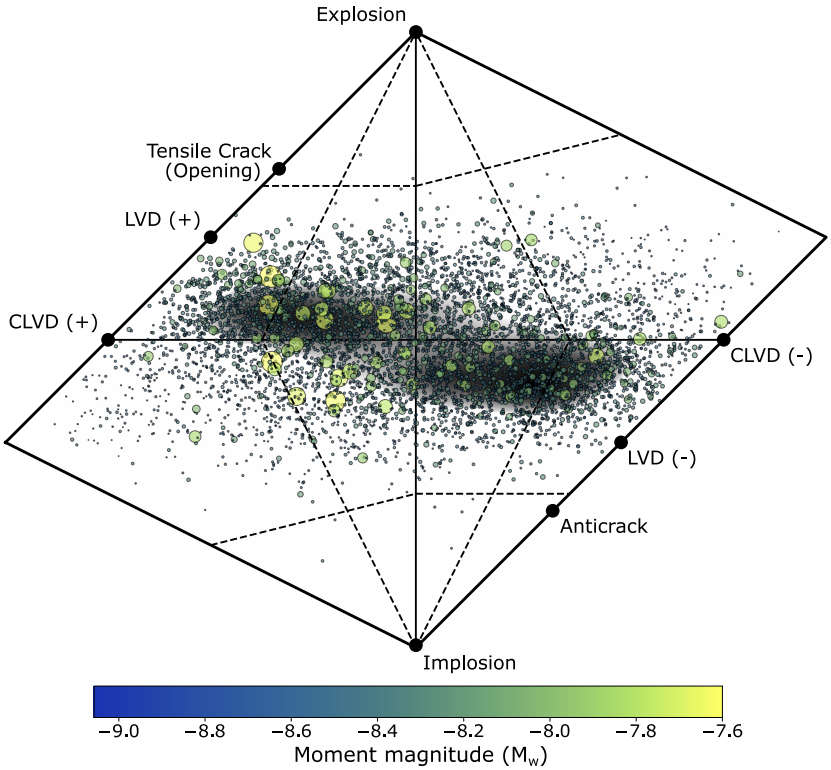

Figure 3 Hudson source type representation of the complete seismic catalogue of test presented in this article. Circles represent detected events, with their size and color corresponding to their moment magnitude (M_w).

4 Spatial-temporal distribution of the AE events and their correlation to the macro-fracture

Figure 5(a) shows the XR-CT of the sample obtained after the test (post failure). Figure 5(b) shows the seismic events prior to failure (t_f), superimposed on the macro-fracture (fault) isolated from the post-test XR-CT (Figure 4(a)). The AEs are coloured by their event time and scaled by their moment magnitude (M_w). The direction of the macro-fracture that caused the failure is indicated by the green arrow, inferred from the spatial-temporal distribution of the AEs. Figure 4(c) shows a virtual 3D reconstruction of the sample deformation. The distributed circumferential strain from the last measurement prior to the stress drop was interpolated and used to colour this virtual reconstruction, following the methodology described in Salazar Vásquez et al (2022). Visually, the localized strain coincides with the eventual location of the macro-fracture, as determined by XR-CT. The spatial correlation between the strain localization and the macro-fracture does not necessarily provide insight into the fracture process, which started long before failure (see section 3 of the main article).

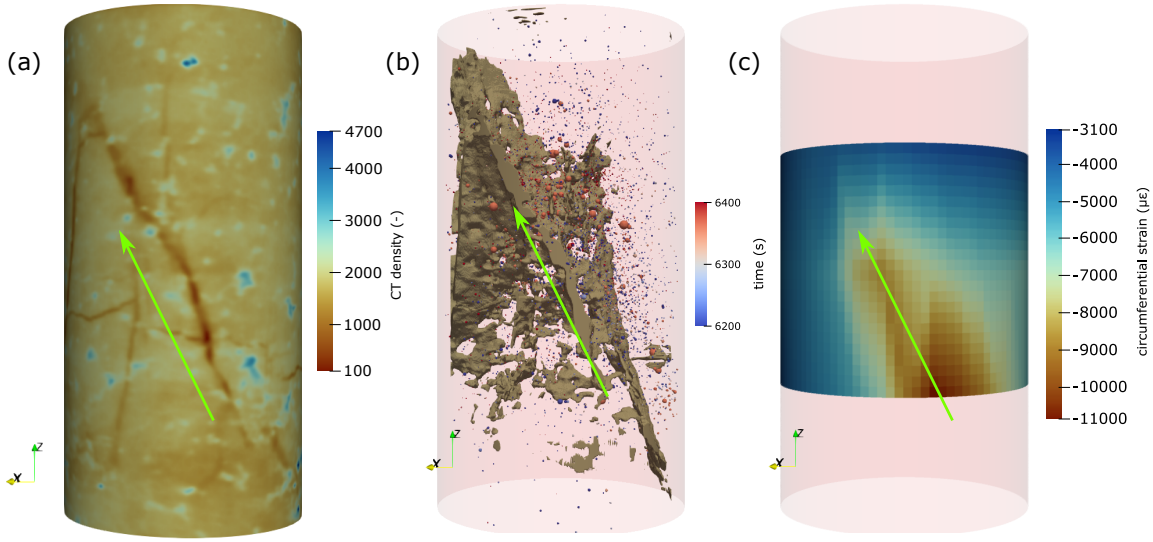

Figure 4 (a) XR-CT of the post-test sample. A comprehensive overview of the post-test sample surface obtained from the XR-CT scan is provided in Supplementary Video 2. (b) AE events prior to the dynamic stress drop are scaled by their moment magnitude (M_w) and superimposed on the macro-fracture network isolated from the XR-CT. (c) The last circumferential strain measurement (at t_f) was interpolated and used to colour a virtual cylindrical sample. All figures are presented from the same orientation. Green arrows indicate the inferred location of the macro-fracture nucleation and its direction of propagation.

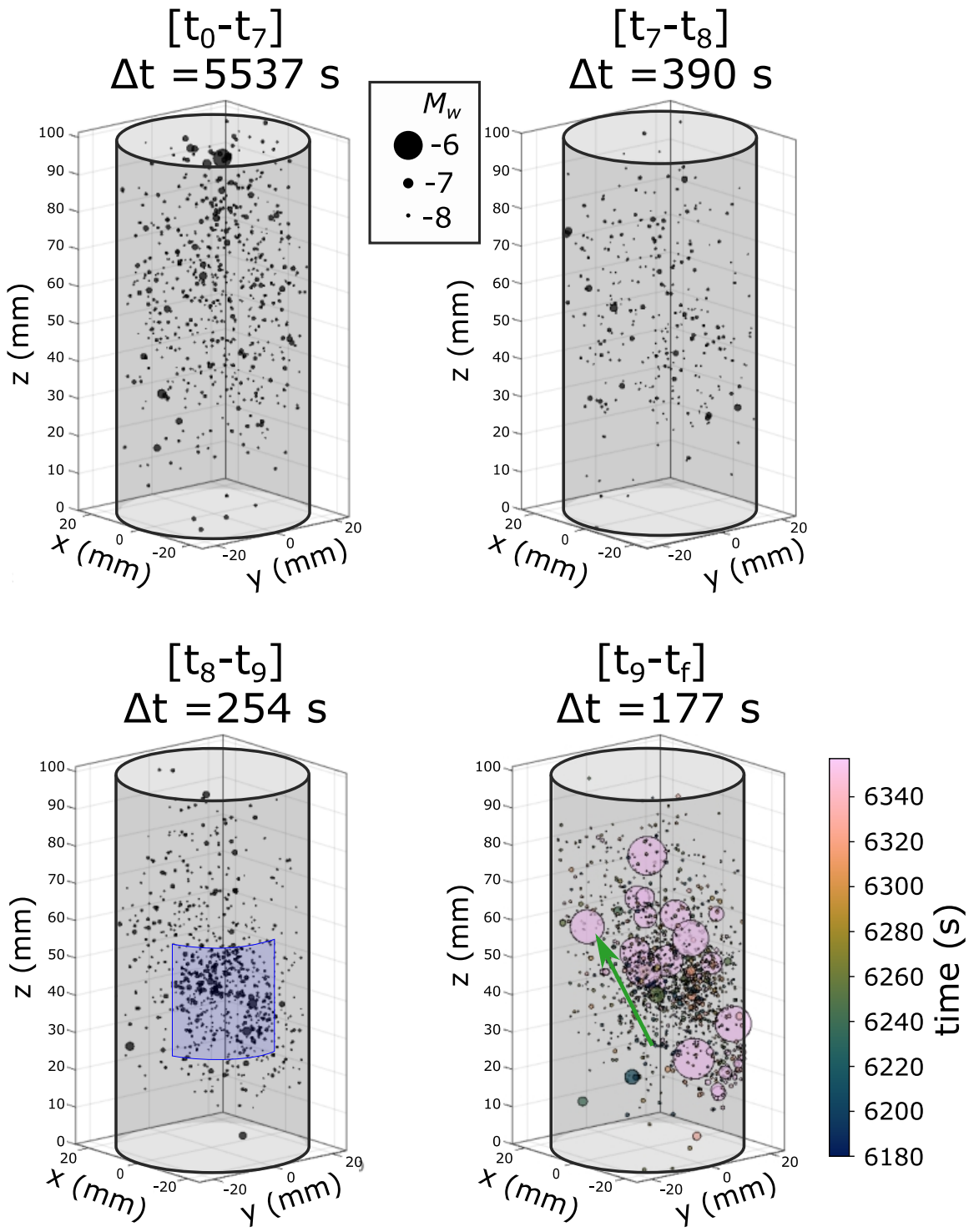

Figure 5 Spatial distribution of the AEs nucleated before failure (t_f). The size of the markers are proportional to the M_w of the events. The AEs in the moments before failure (from t_9 to t_f) are coloured according to their event time.

5 Construction of the 2D histograms

This section describes the methodology used to construct the 2D histogram plots presented in the main article.

Figure 6 illustrates the methodology used to construct the 2D histograms shown in Section 2.4 of the main article. The cylindrical sample was virtually divided into three horizontal volumes, each with an optical fiber segment positioned at its center. These sub-volumes were further divided into arcs and radial segments. The 2D histogram colouring was assigned using the cumulative seismic moment of the AEs nucleated in each voxel. To account for variations in size, the cumulative moment magnitude was corrected by the voxel volume. The continuous black line represents the distributed circumferential strain, with the radial distance corresponding to the measured strain.

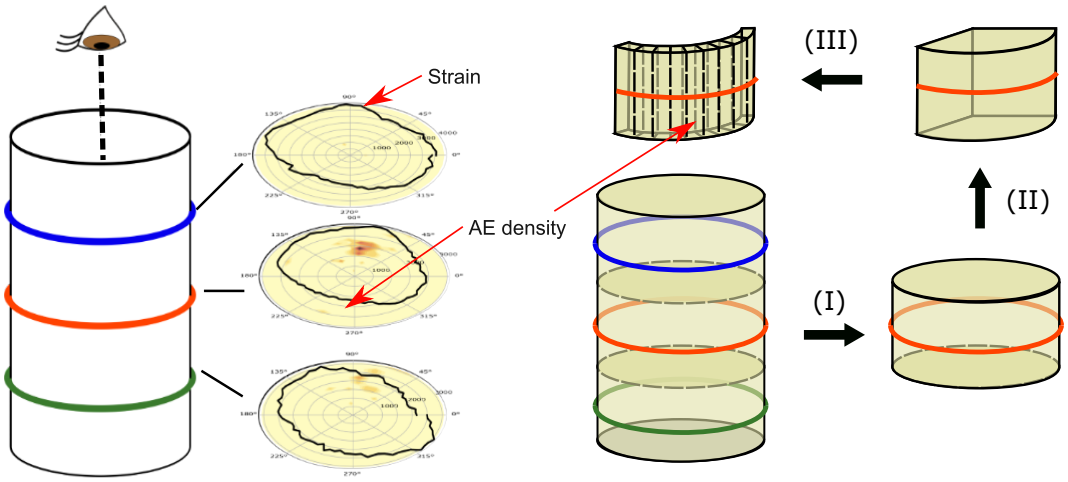

Figure 6 Diagram of the construction of the 2D histograms shown in Section 2.4 of the main article. The sample was divided into sub voxels following the sequences indicated by the black arrows. (I) The volume was divided in tree heights, (II) Each disc was divided in the radial direction, and (III) The arches were further divided in the circumferential direction. The cumulative seismic moment of the AEs nucleated inside each voxel was used to colour the 2D histogram.

6 Seismic tomography

6.1 Methodology

A tomographic survey was performed every 120 seconds, consisting of a loop of active pulses. Each sensor was pulsed ten times before the multiplexer (Elsys HVP-MUX) switched to the next sensor, continuing until all 16 sensors were used. This process allowed us to construct a detailed understanding of the velocity model at various stages of the experiment. Details of the data acquisition system and the high-voltage pulsing unit are provided in section 5.2.2 of the main article and by Selvadurai et al (2022).

The continuous data was first analyzed to separate the active shots from the passive acoustic recordings. Individual active shots were identified using a cross-correlation function and then stacked in time. The P-wave arrival time was initially selected using the Akaike information criterion (AIC; Akaike, 1974) and subsequently manually corrected.

6.2 Results and Discussion

Figure 7 shows an extended view of the the results of the active surveys (see also Figure 1(a) of the main article). The P-wave velocity at each height was calculated from the pair of sensor that transect the eventual macro-fracture horizontally. Across all heights, the P-wave velocity shows an initial increase during the first 1500 s, reaching 4600 m/s in the upper height (purple diamonds). At about 2500 s, the velocity was observed to decrease at a constant rate in the three lower heights (orange, red and green diamonds). Aben et al (2019) measured similar P-wave velocity heterogeneity in a granite sample tested under triaxial conditions, observing an approximately constant P-wave velocity in zones distant from the inferred damage and a decrease of up to 25% in highly damaged zones.

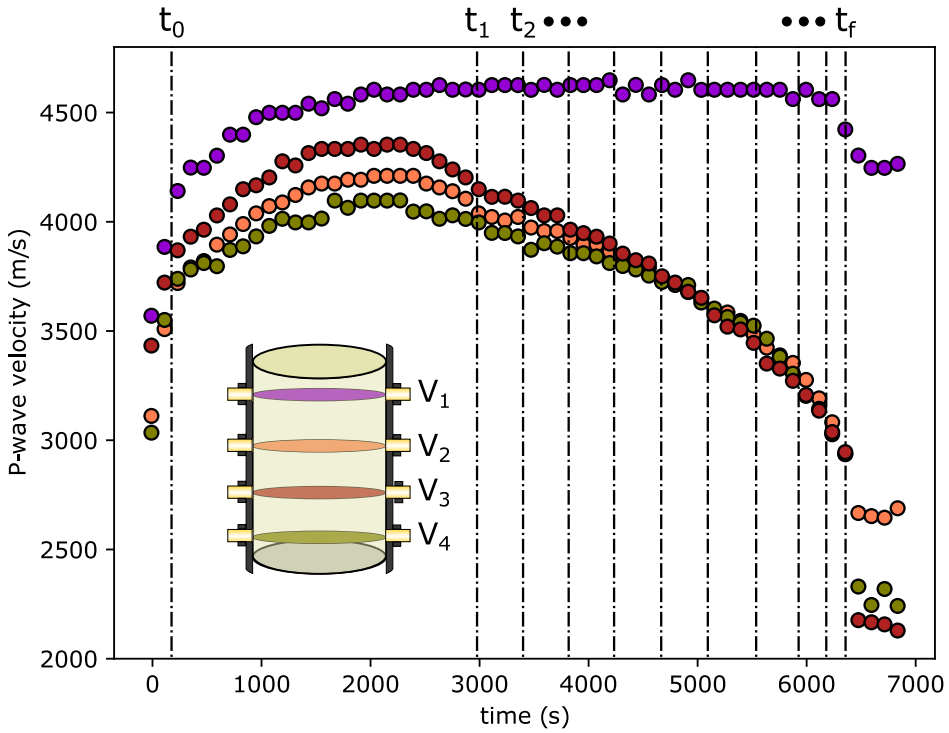

Figure 7 P-wave velocity evolution calculated at four different heights of the sample, with each height represented by the colour code in the small scheme of the sample. Results are obtained from pairs of sensors oriented perpendicular to the nucleated macro-fracture at each height.

The evolution of the average P-wave velocity is shown in Figure 8. The P-wave velocity shows a similar behaviour to that of the volumetric strain (Figure 11(a)), with an initial increase followed by a decrease. During a triaxial test using a confining pressure of 20 MPa, Stanchits et al (2006) measured the P-wave velocity evolution of an Aue granite sample. They did not observe any increase in P-wave velocity during the initial stages of the test. In contrast, we observed an increase of about 0.8 km/s at a differential stress of 150 MPa. This difference could be attributed to a higher density of pre-existing fractures in the Rontondo granite, which were closed by the initial differential stress (Tapponnier and Brace, 1976; Brace, 1978; Wong, 1982). This also explains the initial non-linear contraction observed in the present test (Figure 11(a)), which was found to be linear in the granite sample tested by Stanchits et al (2006). After reaching the peak (approximately at 190 MPa of differential stress), we observed a decrease in P-wave velocity of about 1 km/s (Figure 8), which correlates with the decrease observed by Stanchits et al (2006) and the dilatation of the Rotondo sample (Figure 11). This P-wave decrease may be related to damage produced within the sample, as discussed in section 3.1 of the main article.

Natural fault zones have also exhibited similar decreases in P-wave velocity. For example, Allam and Ben-Zion (2012) and Scott et al (1994) presented tomographic images of crustal structures in the southern California plate boundary, where they observed a P-wave velocity decrease of 25% to 40%

within the fault zone. Cochran et al (2009) reported a P-wave decrease of 40% to 50% in the Calico fault in eastern California. These velocity reductions were associated with post-seismic damage in the active fault zones. In contrast, Figure 7 shows that the P-wave velocity decreases by up to 30% in the fault zone of our sample.

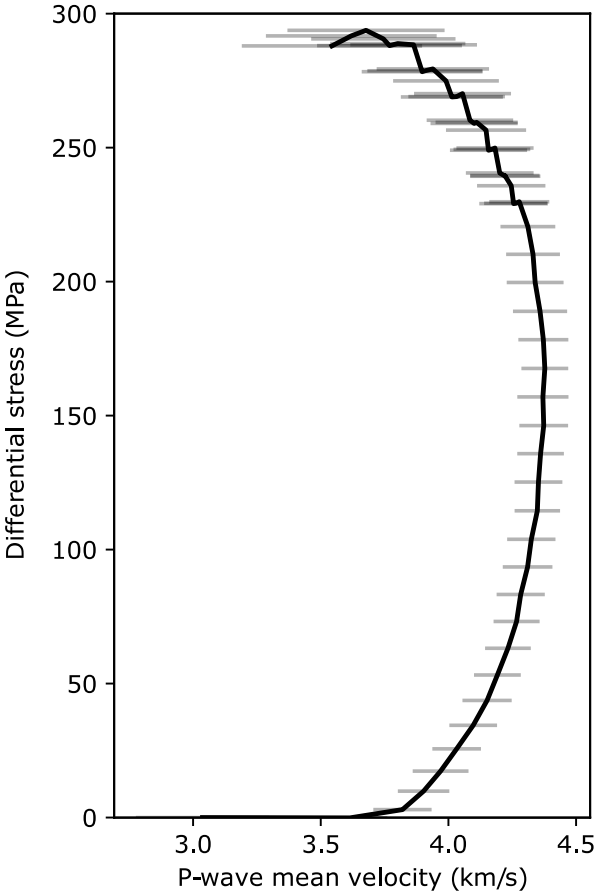

Figure 8 Evolution of the mean P-wave velocity. Error bars represent the standard deviation of the measurements.

7 Seismic and aseismic sensors and equipment

7.1 Distributed strain sensing (DSS)

Figure 9 shows the cross section of the two optical fibers implemented in the present test. The optical fiber selection accounts for two phenomenas: strain lag and light attenuation due to micro-bending. Strain lag arises because thicker and softer coatings impair the strain transfer to the fiber core (Ansari and Libo, 1998; Wang and Zhou, 2014; Billon et al, 2015; Wang and Xiang, 2016; Zhang et al, 2020; Falcetelli et al, 2020; Chapeleau and Bassil, 2021). Light attenuation is a consequence of the bending of the fiber below its critical radius Gardner (1975); Gambling et al (1979); Sun et al (2022). In triaxial systems, micro-bending occurs when the confining pressure forces the fiber against the micron-scale surface roughness, and is also caused by fiber overlap (Salazar Vásquez et al, 2022). The acrylate-coated optical fiber used in this study introduces a strain lag of approximately 4 cm (Salazar Vásquez et al, 2022); however, it mitigates light attenuation problems during high-pressure triaxial testing. In contrast, the use of a thin polyimide-coated fiber reduces the strain lag to a few millimetres, allowing axial strain to be measured in relatively short samples. For more detailed information on the calibration and performance of the DSS method in triaxial rock experiments, we encourage readers to refer to the comprehensive study by Salazar Vásquez et al (2022).

The optical backscatter reflectometer (OBR 4600, Luna Innovations) was used to interrogate the optical fibers. This interrogator is capable of measuring large strains using the incremental post-processing method described by Salazar Vásquez et al (2022). In this study, the DSS system was configured to provide a spatial resolution of 5 mm at a sampling rate of 0.25 Hz.

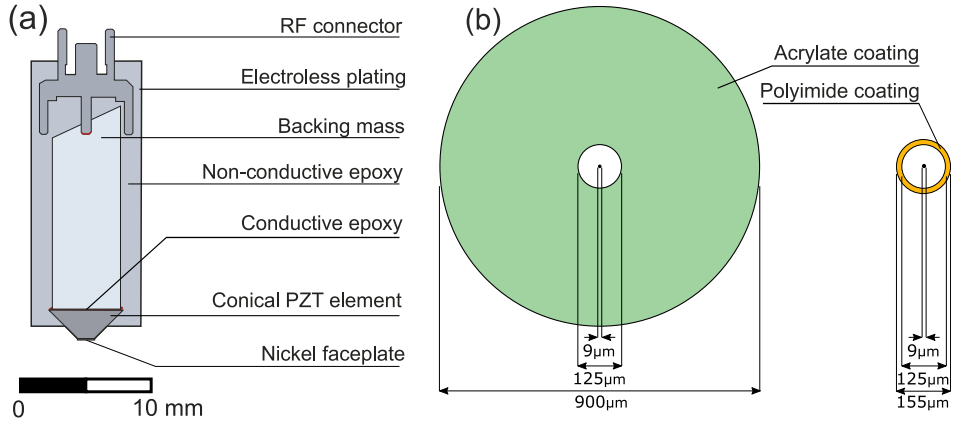

Figure 9 Cross sections of the AE and DSS sensors implemented in this work. (a) Schematic showing the internal structure of the piezoelectric AE sensor (adapted from Selvadurai et al (2022)). (b) Cross sections of the optical fibers: 900 μm diameter acrylate-coated fiber from Solifos AG and 155 μm diameter polyimide-coated fiber from Fibercore (adapted from Salazar Vásquez et al (2022)).

7.2 Acoustic emission (AE)

Figure 9(a) shows a cross-section of the in-house constructed AE sensor used in this study. The sensor follows the design of other point contact transducers (Eitzen et al, 1981; Eitzen and Wadley, 1984;

Glaser et al, 1998). All components were selected to provide a flat frequency response from 70 kHz to 1.5 MHz, minimizing distortion in the physical interpretation of the wave field, while withstanding high pressure and temperature conditions. The piezoelectric crystal in the acoustic lead zirconate titanate (PZT) sensor was shaped as a truncated cone, following the National Institute of Standards and Technology (NIST) specifications for broadband PZT sensors (Eitzen and Wadley, 1984; Proctor et al, 2020). Full details of the components and instrument responses of AE sensors with similar spectral responses can be found in Selvadurai et al (2022).

Each individual AE sensor was calibrated on a transfer plate using capillary tube fracture to generate the source (Breckenridge, 1990; McLaskey and Glaser, 2012; Selvadurai et al, 2022). The calibration procedure compares the electrical signal of the PZT sensor with the theoretical displacement of a dynamic wave generated by a known force excitation and takes advantage of the source-sensor tool chain (Grosse et al, 2021). A standard steel plate was used for the calibration (Wu et al, 2021; Selvadurai et al, 2022) and theoretical Green's functions were calculated using a generalized ray code (Hsu, 1985). Capillary tube fractures were used as a calibration source because they produce larger amplitudes at frequencies above 700 kHz (Breckenridge, 1990). Spectral division was used to determine the instrument response of each sensor, which includes distortions introduced by contact conditions, pre-amplifiers, cables, digitization, etc. The sensor-dependent instrument responses derived from the steel transfer plate were applied directly to the measurements taken inside the triaxial cell. This assumes that the sensor-media coupling (i.e., contact conditions) does not affect the instrument response, a consideration that has been validated in other triaxial experiments (McLaskey et al, 2015; Marty et al, 2023). We assume that the piezoelectric sensors are sensitive to unidirectional ground motion in the poling direction of the piezoelectric crystal and that the sensor instrument responses are relatively insensitive to incident angles below than 55^o (Selvadurai et al, 2022). With the calibrated instrument response, it is possible to give a quantitative interpretation of the AEs nucleated as the sample was driven to failure (e.g., McLaskey and Glaser, 2011; McLaskey et al, 2015; Yoshimitsu et al, 2014; Goodfellow and Young, 2014; Selvadurai, 2019).

During the experiment, each acoustic data channel was continuously sampled (at 10 MHz with 16 bits) using the TraNET EPC data acquisition module (Elsys Instruments AG). Signals were pre-conditioned using analogue preamplifiers with +40 dB gain (Elsys AE-AMP). A loop of active pulses performed a tomographic scan every 120 seconds. Each sensor was pulsed ten times before the multiplexer (Elsys HVP-MUX) switched to the next sensor, continuing until all 16 sensors were used. This process allowed to construct a detailed velocity model at various stages of the experiment. Further details on the data reduction of the AE data are provided in the main article. Details of the data acquisition system and the high-voltage pulsing unit can be found in Selvadurai et al (2022).

Figure 10(a) shows the sample instrumented with the optical fibers. The layout of the DSS and AE sensors is shown in Figure 10(b). Figure 10(c) shows the jacketed sample mounted in the triaxial device before testing (Figure 10(c)).

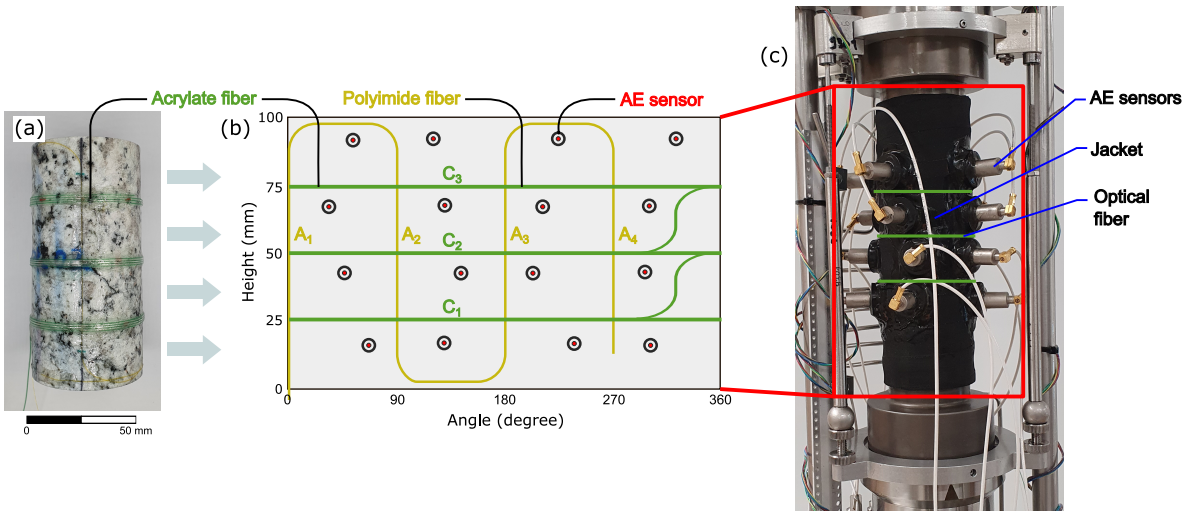

Figure 10 (a) Sample implemented with both types of optical fibers before jacketing. (b) Unwrapped surface of the sample with the location of the implemented AE and DSS sensors. The polyimide-coated fiber (yellow) was overlapped by the acrylate-coated fiber (green). (c) Sample mounted in the triaxial device before testing. Green lines are superimposed on the picture to indicate the positions of the circumferential wrapping of the optical fiber.

8 Volumetric strain and seismic energy

A comparison between the evolution of the average volumetric strain and the cumulative moment ($\sum M_0$) is shown in Figure 11. The error bars in Figure 11(a) represent the maximum and minimum of the distributed volumetric strain. The volumetric strain is consistent with that observed in low porosity rock (Brace, 1978). During the first part of the test, the sample undergoes a reduction in volume (contraction) with an initial non-linear growth, followed by a linear increase. At approximately 65% of the peak differential stress (190.5 MPa), the average volumetric strain deviates from the linear behavior (C'). Following this, the sample experiences an increase in volume (dilation) with exponential growth toward failure. The increase in dispersion in the error bars was driven by the onset of localized strain (Figure 1(c) in the main article).

As expected from the initial seismic quiescence (Figure 3 in the main article), a low cumulative seismic moment was observed during the initial stages of the test (Figure **??**(b)). An increase in the cumulative moment was initiated around C'. However, more than 60% of the seismic energy was measured in the last 400 seconds before failure ($t_8 - t_f$)

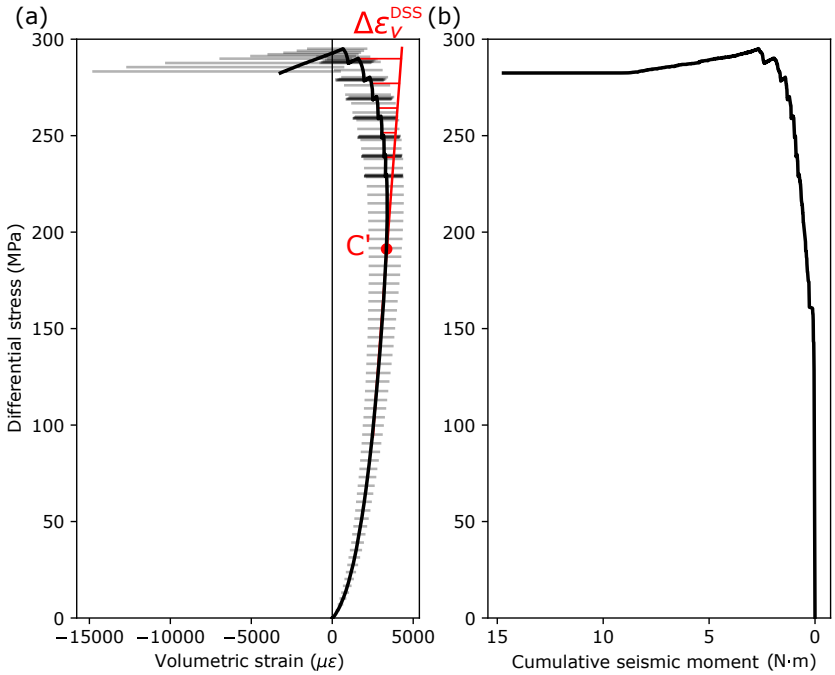

Figure 11 (a) Volumetric strain evolution. The total anelastic volumetric strain ($\Delta\varepsilon_V^{DSS}$) is defined as the difference between the volumetric strain and the projection of the elastic part (red line). C' (represented by the red dot) marks the point where the volumetric strain deviates from the linear-elastic behavior. Error bars indicate the maximum and minimum volumetric strain measured on the sample's surface. (b) Evolution of the cumulative seismic moment (M_0). The x-axis has been inverted for comparison.

9 Frequency magnitude distribution: Parameter selection and sensitivity analysis

9.1 Selection of the parameters

Diverse methods have been employed to obtain the magnitude of completeness (M_c') of the frequency-magnitude distribution (FMD) of a seismic catalogue, including visual inspection Wiemer and Wyss (2000, 2002). We took a quantitative methodology to ascertain M_c' and bin size (δ). This involved conducting a sweep analysis using the entire dataset. For each pairing of M_c' and δ, we calculated the synthetic distribution with slope van der Elst (2021),

$$\hat{\beta} = \frac{1}{\delta \cdot ln(10)} \coth^{-1}\left(\frac{1}{\delta}\bar{M}_w' - M_c' + \delta\right). \tag{1}$$

The goodness of the fit between the FMD of the seimis catalog and the synthetic distribution was assessed using the coefficient of determination (Wiemer and Wyss, 2002)

$$R = 100 - \left(\frac{\sum_{M_i'}^{M_{max}'}(|B_i - S_i|)}{\sum_i B_i}100\right), \tag{2}$$

where B_i and S_i are the observed and predicted cumulative number of AE events in each bin. Following Wiemer and Wyss (2002), we used $R > 90\%$ as the criterion for a good fit.

Figure 12 show four examples of the sweep analysis using (a) δ=0.01, (b) δ=0.02, (c) δ=0.03 and (d) δ=0.04. For δ greater or equal to 0.04, R is below 90% for all M_c'. Better fits (i.e., larger R) are obtained when using smaller bin sizes. Larger M_c' also results in better fits; however, this excludes a larger number of AEs.

We selected δ=0.01 and M_c'=0.07 (red square in Figure 12(a)) because this combinations provides a good fit (R >90%; Wiemer and Wyss (2002)) while excluding the fewest number of AEs.

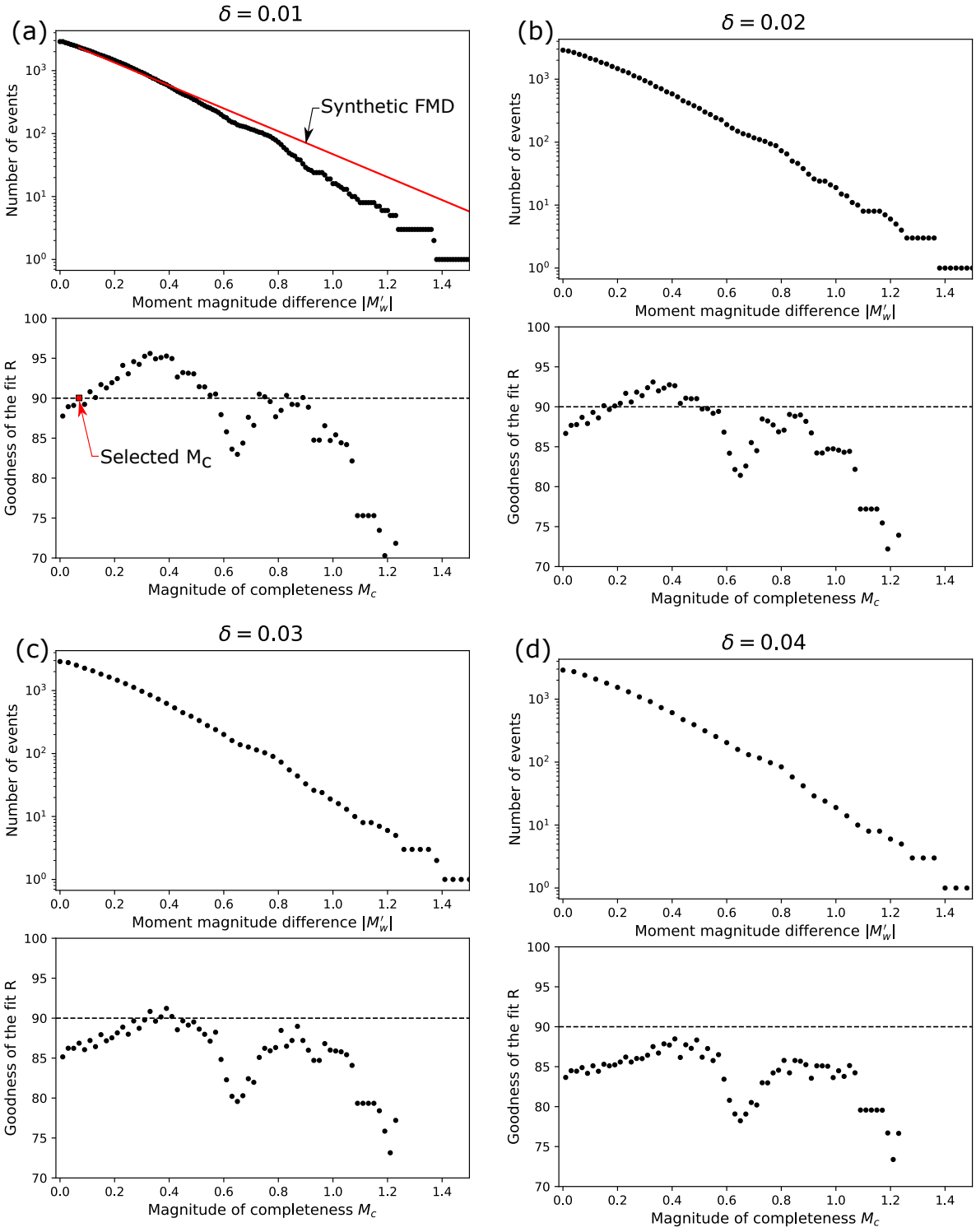

Figure 12 Examples of the sweep analysis for the magnitude of completeness (M_c') and bin size (δ): (a) δ=0.01, (b) δ=0.02, (c) δ=0.03 and (d) δ=0.04. The coefficient of determination (R; lower graphs) was calculate to determined goodness of the fit. The red line in (a) represents the synthetic magnitude difference distribution for the entire catalogue, while the red square indicates the selected combination of M_c' and δ.

9.2 Sensitivity analysis

9.2.1 Sub-cluster size

This sensitivity analysis considered two different sub-cluster sizes: 240 and 800 AE events. Figures 13 and 14 show the temporal fluctuations of the b- and D-values for the two sub-cluster sizes. The fluctuations of the b- and D-values are similar to the analysis performed using 480 events (see Figure 3(d) in the main article). In all cases, we observed two b-value decreases during the last 200 seconds before failure, with the minimum b-value recorded just after t_f. Only slight differences in the b-value magnitude were observed between the two sub-cluster sizes throughout the test.

The fluctuations of the D-value, calculated using sub-cluster sizes of 240 and 800 AE events (Figure 14), are also similar to the ones obtained using 480 events (see Figure 3(e) in the main article). The periods of localization, delocalization, re-localization, and re-delocalization are conserved using different cluster sizes. Nevertheless, slight variations in the timing of these pronounced fluctuations were observed.

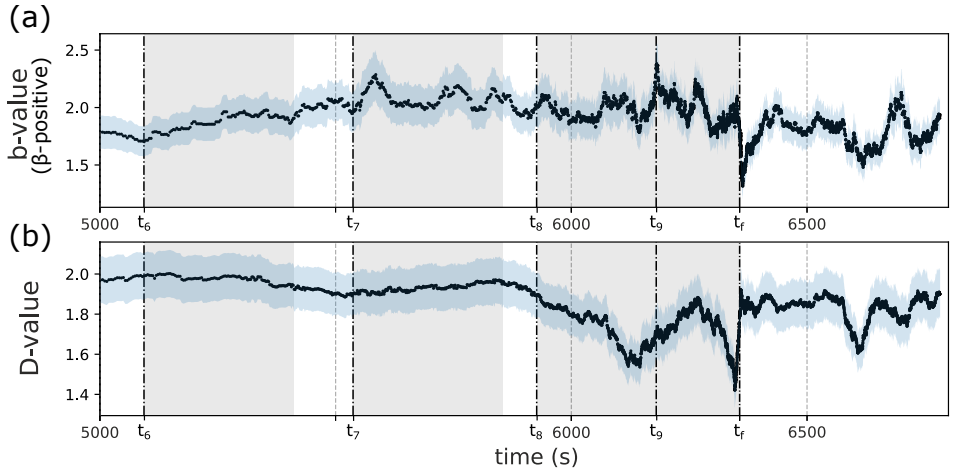

Figure 13 Temporal fluctuations of the (a) b-value and (b) D-value during the tests. (b) Spatial statistics of the AE events using the D-value. The b- and D-values were calculated using a running sub-catalogue of 240 events. Regions coloured in light grey indicate the holding phases, while regions in light blue represent the estimated error (see Section 4.5.3. in the main article).

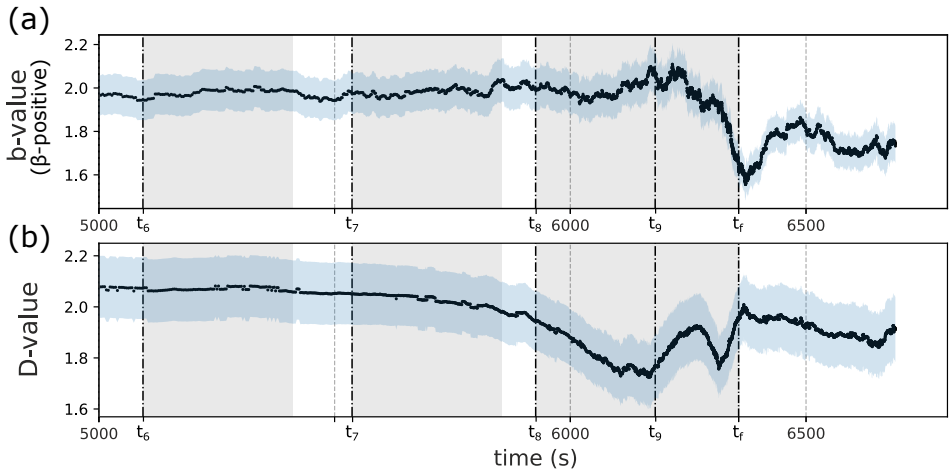

Figure 14 Temporal fluctuations of the (a) *b*-value and (b) D-value during the tests. (b) Spatial statistics of the AE events using the D-value. The b- and D-values were calculated using a running sub-catalogue of 800 events. Regions coloured in light grey indicate the holding phases, while regions in light blue represent the estimated error (see Section 5.5.3. of the main article).

Figures 15 and 16 show the correlation of the *b*-value with the average volumetric strain ((a); $\dot{\bar{\varepsilon}}_v$) and the standard deviation of the volumetric strain rate ((b); $\sigma_{\dot{\varepsilon}_v}$) for sub-cluster sizes of 240 and 800, respectively. The inverse correlation is maintained when using larger or smaller sub-clusters sizes.

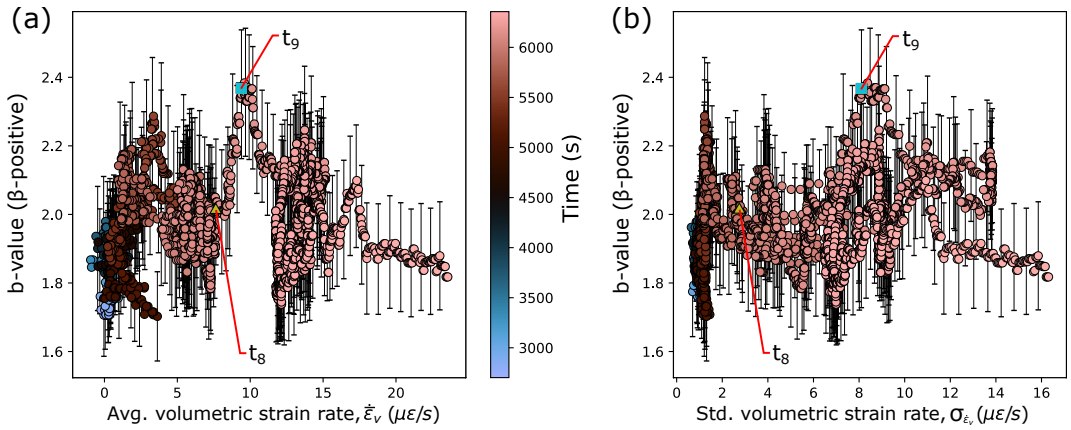

Figure 15 Fluctuation of *b*-value with (a) average volumetric strain rate $\dot{\bar{\varepsilon}}_v$ and (b) standard deviation of the volumetric strain rate $\sigma_{\dot{\varepsilon}_v}$, using a sub-cluster size of 240 events. The colour indicates time of the test. $\dot{\bar{\varepsilon}}_v$ and $\sigma_{\dot{\varepsilon}_v}$ were linearly interpolated to match the time stamps of the *b*-value.

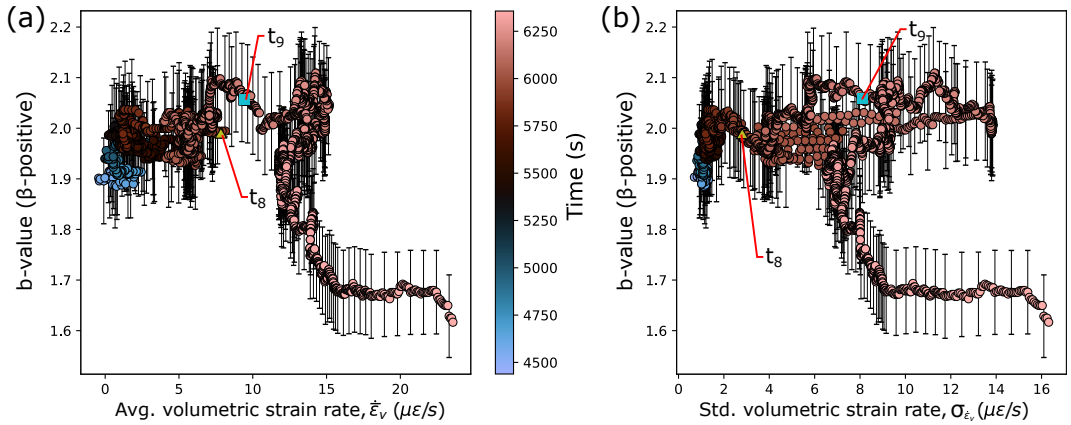

Figure 16 Fluctuation of b-value with (a) average volumetric strain rate $\dot{\bar{\varepsilon}}_v$ and (b) standard deviation of the volumetric strain rate $\sigma_{\dot{\varepsilon}_v}$, using a sub-cluster size of 800 events. The colour indicates time of the test. $\dot{\bar{\varepsilon}}_v$ and $\sigma_{\dot{\varepsilon}_v}$ were linearly interpolated to match the time stamps of the b-value.

9.2.2 Magnitude of completeness (M_c') and bin size (δ)

Figure 17(a) compares the fluctuations of the b-value when using higher and lower M_c' while maintaining the same δ. In Figure 17(b), the bin size was varied while keeping the same M_c'. Lower b-values were obtained when using larger δ, though the overall shape of the fluctuations remained consistent. Significant deviations in the b-value become apparent with variations in M_c'. For example, lower or larger b-value was obtained at t_9 when different M_c' were used (Figure 17(a)).

Figure 17(c) compares the b-value fluctuation when using the parameters selected in section 9.1 ($M_c' = 0.07$ & $\delta = 0.01$) with those from the parameters that showed the highest R (Section 9.1). The fluctuations in the b-value become more pronounced when using larger M_c', which can be attributed to the smaller sub-catalog associated with higher M_c'.

Despite the variations in the b-value responses presented in this section, the principal trends discussed in the main article remain consistent. For all pairs of M_c' and δ shown in Figure 17, an increase of the b-value was observed close to t_9. This was followed by two distinct decrease in the b-value as the sample approached failure.

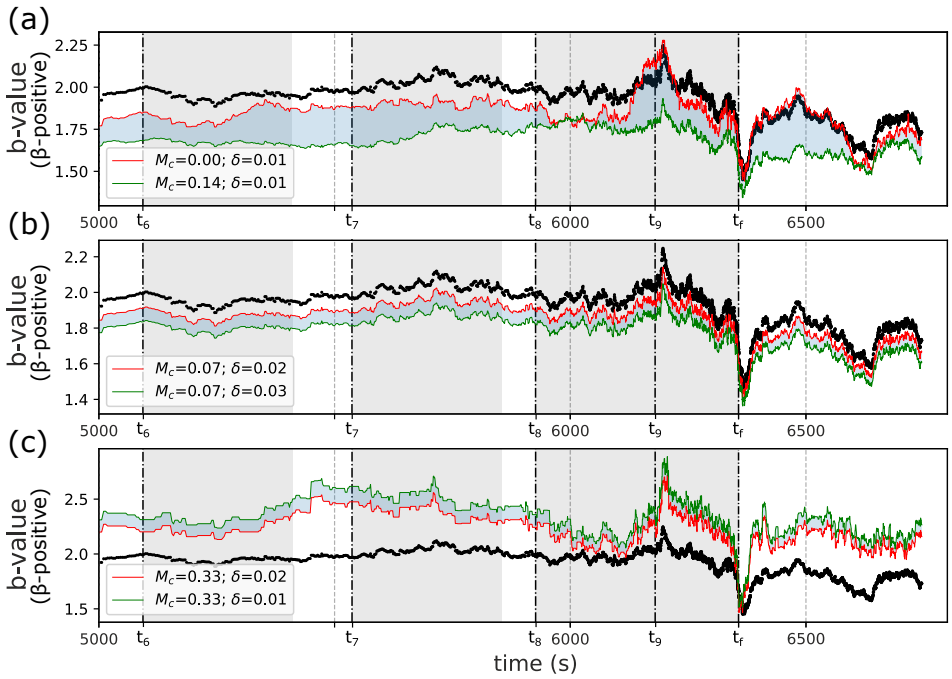

Figure 17 Sensitivity analysis of the magnitude of completeness M_c' and bin size δ. The b-value presented as black dots were obtained using the same parameters as in the main article ($M_c' = 0.16$; $\delta = 0.02$). (a) b-value comparison using different M_c' with a constant δ. (b) b-value comparison using different δ with a constant M_c'. (c) b-value comparison using different M_c' and δ.

An important observation in the main article is that the b-value exhibits an inverse correlation with both the average volumetric strain ($\dot{\bar{\varepsilon}}_v$) and the the standard deviation of the volumetric strain rate ($\sigma_{\dot{\varepsilon}_v}$). Figures 18 and 19 show that these inverse correlations persists in all pairings of M_c' and δ.

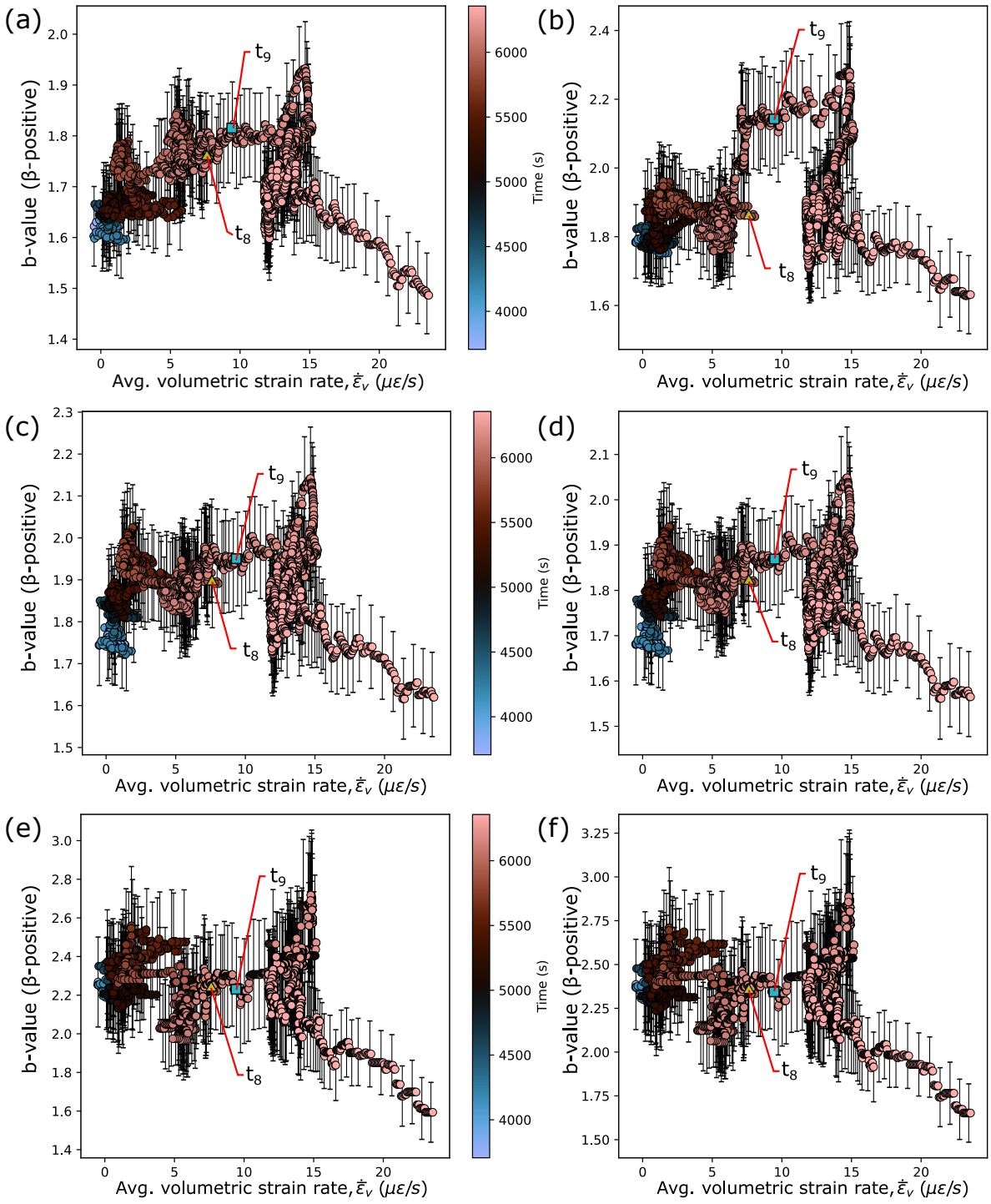

Figure 18 Fluctuation of b-value with average volumetric strain rate $\dot{\varepsilon}_v$. The colour indicates the time of the test. The b-value was calculated using the following pair of parameters: (a) $M_c' = 0.0$ & $\delta = 0.01$, (b) $M_c' = 0.14$ & $\delta = 0.01$, (c) $M_c' = 0.07$ & $\delta = 0.02$, (d) $M_c' = 0.07$ & $\delta = 0.03$, (e) $M_c' = 0.33$ & $\delta = 0.02$ and (f) $M_c' = 0.33$ & $\delta = 0.01$.

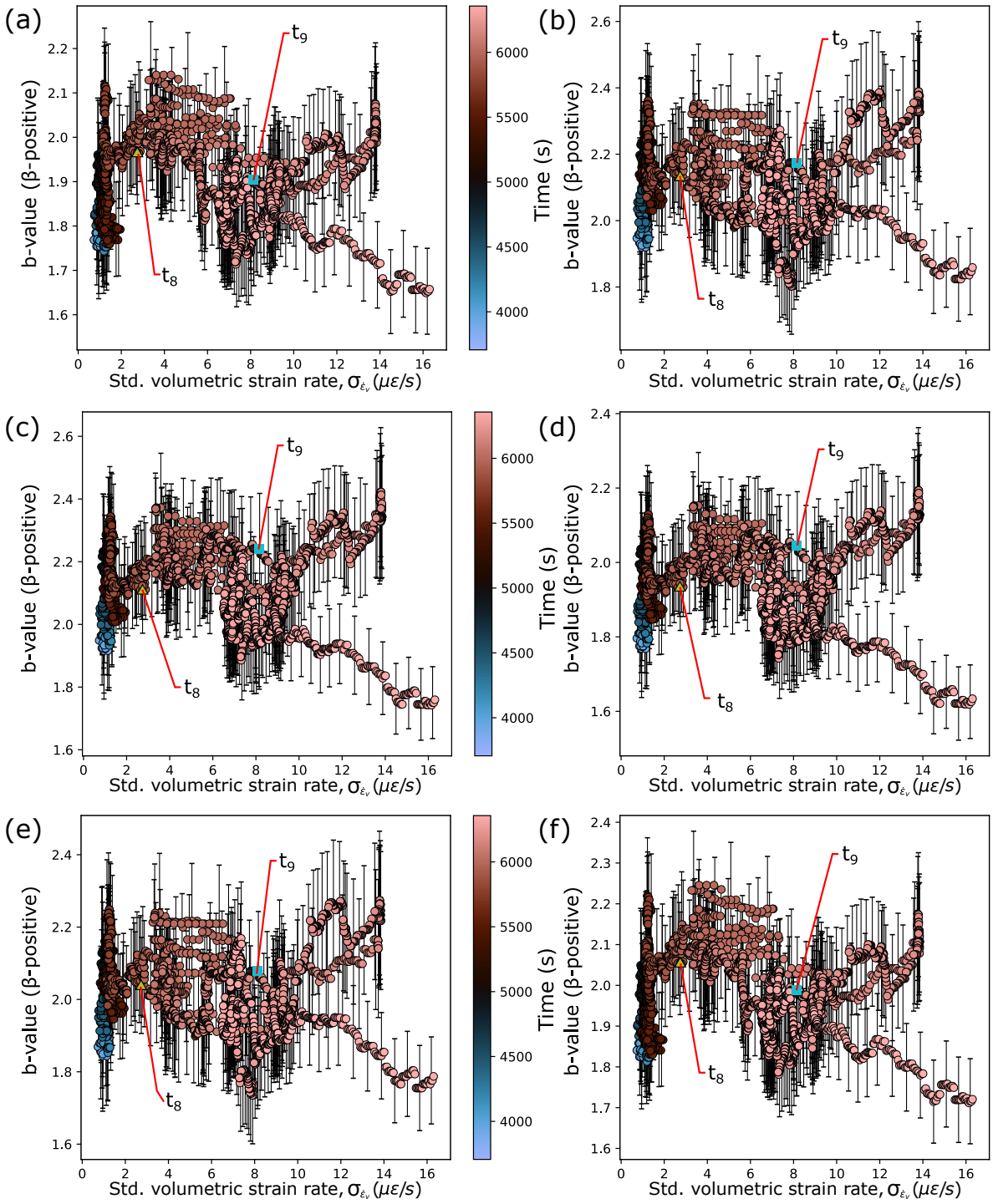

Figure 19 Fluctuation of b-value with the standard deviation of the volumetric strain rate $\sigma_{\dot{\varepsilon}_v}$. The colour indicates the time of the test. The b-value was calculated using the following pair of parameters: (a) $M_c' = 0.1$ & $\delta = 0.02$, (b) $M_c' = 0.2$ & $\delta = 0.02$, (c) $M_c' = 0.16$ & $\delta = 0.01$, (d) $M_c' = 0.16$ & $\delta = 0.03$, (e) $M_c' = 0.2$ & $\delta = 0.03$ and (f) $M_c' = 0.1$ & $\delta = 0.01$.

References

Aben FM, Brantut N, Mitchell TM, et al (2019) Rupture energetics in crustal rock from laboratory-scale seismic tomography. Geophysical Research Letters 46(13):7337–7344. https://doi.org/https://doi.org/10.1029/2019GL083040, URL https://agupubs.onlinelibrary.wiley.com/doi/abs/10.1029/2019GL083040, https://agupubs.onlinelibrary.wiley.com/doi/pdf/10.1029/2019GL083040

Akaike H (1974) A new look at the statistical model identification. IEEE transactions on automatic control 19(6):716–723

Allam AA, Ben-Zion Y (2012) Seismic velocity structures in the southern California plate-boundary environment from double-difference tomography. Geophysical Journal International 190(2):1181–1196. https://doi.org/10.1111/j.1365-246X.2012.05544.x, URL https://doi.org/10.1111/j.1365-246X.2012.05544.x, https://academic.oup.com/gji/article-pdf/190/2/1181/17364795/190-2-1181.pdf

Ansari F, Libo Y (1998) Mechanics of Bond and Interface Shear Transfer in Optical Fiber Sensors. Journal of Engineering Mechanics 124(4):385–394. https://doi.org/10.1061/(ASCE)0733-9399(1998)124:4(385)

Billon A, Hénault JM, Quiertant M, et al (2015) Qualification of a distributed optical fiber sensor bonded to the surface of a concrete structure: a methodology to obtain quantitative strain measurements. Smart Materials and Structures 24(11):115001. https://doi.org/10.1088/0964-1726/24/11/115001, URL https://doi.org/10.1088/0964-1726/24/11/115001

Brace WF (1978) Volume changes during fracture and frictional sliding: A review. pure and applied geophysics 116(4):603–614. https://doi.org/10.1007/BF00876527, URL https://doi.org/10.1007/BF00876527

Breckenridge F (1990) Transient sources for acoustic emission work. Progress in acoustic emission pp 20–37. URL https://ci.nii.ac.jp/naid/10006638702/en/

Chapeleau X, Bassil A (2021) A General Solution to Determine Strain Profile in the Core of Distributed Fiber Optic Sensors under Any Arbitrary Strain Fields. Sensors 21(16). https://doi.org/10.3390/s21165423, URL https://www.mdpi.com/1424-8220/21/16/5423

Cochran ES, Li YG, Shearer PM, et al (2009) Seismic and geodetic evidence for extensive, long-lived fault damage zones. Geology 37(4):315–318. https://doi.org/10.1130/G25306A.1, URL https://doi.org/10.1130/G25306A.1, https://pubs.geoscienceworld.org/gsa/geology/article-pdf/37/4/315/3536256/i0091-7613-37-4-315.pdf

David C, Nejati M, Geremia D (2020) On petrophysical and geomechanical properties of Bedretto Granite. Tech. rep., Zurich, https://doi.org/10.3929/ethz-b-000428267

Dong L, Zhang Y, Ma J (2020) Micro-crack mechanism in the fracture evolution of saturated granite and enlightenment to the precursors of instability. Sensors 20(16). https://doi.org/10.3390/s20164595, URL https://www.mdpi.com/1424-8220/20/16/4595

Eitzen D, Wadley H (1984) Acoustic emission: establishing the fundamentals. Journal of research of the National Bureau of Standards 89(1):75–100

Eitzen D, Breckenridge F, Clough R, et al (1981) Summary of fundamental developments for quantitative acoustic emission measurements. Report, National Bureau of Standards, Washington, DC (USA)

van der Elst NJ (2021) B-Positive: A Robust Estimator of Aftershock Magnitude Distribution in Transiently Incomplete Catalogs. Journal of Geophysical Research: Solid Earth 126(2):e2020JB021027. https://doi.org/https://doi.org/10.1029/2020JB021027, URL https://agupubs.onlinelibrary.wiley.com/doi/abs/10.1029/2020JB021027, e2020JB021027 2020JB021027, https://agupubs.onlinelibrary.wiley.com/doi/pdf/10.1029/2020JB021027

Falcetelli F, Rossi L, Di Sante R, et al (2020) Strain Transfer in Surface-Bonded Optical Fiber Sensors. Sensors 20(11). https://doi.org/10.3390/s20113100, URL https://www.mdpi.com/1424-8220/20/11/3100

Feignier B, Young RP (1992) Moment tensor inversion of induced microseisnmic events: Evidence of non-shear failures in the -4 < m < -2 moment magnitude range. Geophysical Research Letters 19(14):1503–1506. https://doi.org/https://doi.org/10.1029/92GL01130, URL https://agupubs.onlinelibrary.wiley.com/doi/abs/10.1029/92GL01130, https://agupubs.onlinelibrary.wiley.com/doi/pdf/10.1029/92GL01130

Gambling WA, Matsumura H, Ragdale CM (1979) Curvature and microbending losses in single-mode optical fibres. Optical and Quantum Electronics 11(1):43–59. https://doi.org/10.1007/BF00624057

Gardner WB (1975) Microbending loss in optical fibers. The Bell System Technical Journal 54(2):457–465. https://doi.org/10.1002/j.1538-7305.1975.tb02848.x

Glaser SD, Weiss GG, Johnson LR (1998) Body waves recorded inside an elastic half-space by an embedded, wideband velocity sensor. The Journal of the Acoustical Society of America 104(3):1404–1412

Goodfellow SD, Young RP (2014) A laboratory acoustic emission experiment under in situ conditions. Geophysical Research Letters 41(10):3422–3430. https://doi.org/https://doi.org/10.1002/2014GL059965, URL https://agupubs.onlinelibrary.wiley.com/doi/abs/10.1002/2014GL059965, https://agupubs.onlinelibrary.wiley.com/doi/pdf/10.1002/2014GL059965

Grosse CU, Ohtsu M, Aggelis DG, et al (2021) Acoustic emission testing: Basics for research–applications in engineering. Springer Nature

Hafner S (1958) Petrographie des südwestlichen Gotthardmassivs zwischen St.Gotthardpass und Nufenenpass. PhD thesis, ETH Zürich, Zürich, https://doi.org/10.3929/ethz-a-000097546, sA aus: Schweizerische Mineralogische und Petrographische Mitteilungen, Band 38, Heft 2, S.255-362. Diss. Naturwiss. ETH Zürich, Nr. 2831, 0000. Ref.: Burri, C. ; Korref.: Laves, F..

Hsu NN (1985) Dynamic Green's functions of an infinite plate: A computer program. National Bureau of Standards, Center for Manufacturing Engineering, Gaithersburg

Hudson JA, Pearce RG, Rogers RM (1989) Source type plot for inversion of the moment tensor. Journal of Geophysical Research: Solid Earth 94(B1):765–774. https://doi.org/https://doi.org/10.1029/JB094iB01p00765, URL https://agupubs.onlinelibrary.wiley.com/doi/abs/10.1029/JB094iB01p00765, https://agupubs.onlinelibrary.wiley.com/doi/pdf/10.1029/JB094iB01p00765

Kwiatek G, Charalampidou EM, Dresen G, et al (2014) An improved method for seismic moment tensor inversion of acoustic emissions through assessment of sensor coupling and sensitivity to incidence angle. International Journal of Rock Mechanics and Mining Sciences 65:153–161. https://doi.org/https://doi.org/10.1016/j.ijrmms.2013.11.005, URL https://www.sciencedirect.com/science/article/pii/S1365160913001809

Labhart T (2005) Erläuterungen zum geologischen atlas der schweiz 1: 25000. Val Bedretto, Atlasblatt 68

Marty S, Schubnel A, Bhat HS, et al (2023) Nucleation of laboratory earthquakes: Quantitative analysis and scalings. Journal of Geophysical Research: Solid Earth 128(3):e2022JB026294. https://doi.org/https://doi.org/10.1029/2022JB026294, URL https://agupubs.onlinelibrary.wiley.com/doi/abs/10.1029/2022JB026294, e2022JB026294 2022JB026294, https://agupubs.onlinelibrary.wiley.com/doi/pdf/10.1029/2022JB026294

McLaskey GC, Glaser SD (2011) Micromechanics of asperity rupture during laboratory stick slip experiments. Geophysical Research Letters 38(12). https://doi.org/https://doi.org/10.1029/2011GL047507, URL https://agupubs.onlinelibrary.wiley.com/doi/abs/10.1029/2011GL047507, https://agupubs.onlinelibrary.wiley.com/doi/pdf/10.1029/2011GL047507

McLaskey GC, Glaser SD (2012) Acoustic emission sensor calibration for absolute source measurements. Journal of Nondestructive Evaluation 31(2):157–168. https://doi.org/10.1007/s10921-012-0131-2

McLaskey GC, Kilgore BD, Beeler NM (2015) Slip-pulse rupture behavior on a 2 m granite fault. Geophysical Research Letters 42(17):7039–7045. https://doi.org/https://doi.org/10.1002/2015GL065207, URL https://agupubs.onlinelibrary.wiley.com/doi/abs/10.1002/2015GL065207, https://agupubs.onlinelibrary.wiley.com/doi/pdf/10.1002/2015GL065207

Proctor B, Lockner DA, Kilgore B, et al (2020) Direct evidence for fluid pressure, dilatancy, and compaction affecting slip in isolated faults. Geophysical Research Letters 47(16):e2019GL086767

Rast M (2020) Geology, Geochronology and Rock Magnetics Along Bedretto Tunnel (Gotthard Massif, Central Alps) and Numerical Modelling of Quartz-Biotite Aggregates

Salazar Vásquez AF, Rabaiotti C, Germanovich LN, et al (2022) Distributed Fiber Optics Measurements of Rock Deformation and Failure in Triaxial Tests. Journal of Geophysical Research: Solid Earth 127(8):e2022JB023997. https://doi.org/https://doi.org/10.1029/2022JB023997, URL https://agupubs.onlinelibrary.wiley.com/doi/abs/10.1029/2022JB023997,

https://agupubs.onlinelibrary.wiley.com/doi/pdf/10.1029/2022JB023997

Scott JS, Masters TG, Vernon FL (1994) 3-D velocity structure of the San Jacinto fault zone near Anza, California—I. P waves. Geophysical Journal International 119(2):611–626. https://doi.org/10.1111/j.1365-246X.1994.tb00145.x, URL https://doi.org/10.1111/j.1365-246X.1994.tb00145.x, https://academic.oup.com/gji/article-pdf/119/2/611/2060581/119-2-611.pdf

Selvadurai PA (2019) Laboratory Insight Into Seismic Estimates of Energy Partitioning During Dynamic Rupture: An Observable Scaling Breakdown. Journal of Geophysical Research: Solid Earth 124(11):11350–11379. https://doi.org/https://doi.org/10.1029/2018JB017194, URL https://agupubs.onlinelibrary.wiley.com/doi/abs/10.1029/2018JB017194

Selvadurai PA, Wu R, Bianchi P, et al (2022) A Methodology for Reconstructing Source Properties of a Conical Piezoelectric Actuator Using Array-Based Methods. Journal of Nondestructive Evaluation 41(1):23. https://doi.org/10.1007/s10921-022-00853-6, URL https://doi.org/10.1007/s10921-022-00853-6

Stanchits S, Vinciguerra S, Dresen G (2006) Ultrasonic Velocities, Acoustic Emission Characteristics and Crack Damage of Basalt and Granite. pure and applied geophysics 163(5):975–994. https://doi.org/10.1007/s00024-006-0059-5, URL https://doi.org/10.1007/s00024-006-0059-5

Steck A (1976) Albit−Oligoklas−Mineralgesellschaften der Peristeritlücke aus alpinmetamorphen Granitgneisen des Gotthardmassivs. Schweizerische Mineralogische und Petrographische Mitteilungen 56:269–292

Sun X, Zhang L, Zeng L, et al (2022) Micro-bending sensing based on single-mode fiber spliced multimode fiber Bragg grating structure. Optics Communications 505:127513. https://doi.org/https://doi.org/10.1016/j.optcom.2021.127513

Tapponnier P, Brace W (1976) Development of stress-induced microcracks in Westerly Granite. International Journal of Rock Mechanics and Mining Sciences & Geomechanics Abstracts 13(4):103–112. https://doi.org/https://doi.org/10.1016/0148-9062(76)91937-9, URL https://www.sciencedirect.com/science/article/pii/0148906276919379

Wang H, Xiang P (2016) Strain transfer analysis of optical fiber based sensors embedded in an asphalt pavement structure. Measurement Science and Technology 27(7):075106. https://doi.org/10.1088/0957-0233/27/7/075106, URL https://doi.org/10.1088/0957-0233/27/7/075106

Wang H, Zhou Z (2014) Advances of strain transfer analysis of optical fibre sensors. Pacific Science Review 16(1):8–18. https://doi.org/https://doi.org/10.1016/j.pscr.2014.08.002, URL https://www.sciencedirect.com/science/article/pii/S1229545014000035

Wiemer S, Wyss M (2000) Minimum Magnitude of Completeness in Earthquake Catalogs: Examples from Alaska, the Western United States, and Japan. Bulletin of the Seismological Society of America 90(4):859–869. https://doi.org/10.1785/0119990114, URL https://doi.org/10.1785/0119990114, https://pubs.geoscienceworld.org/ssa/bssa/article-pdf/90/4/859/2711269/859_ssa99114.pdf

Wiemer S, Wyss M (2002) Mapping spatial variability of the frequency-magnitude distribution of earthquakes. Advances in Geophysics, vol 45. Elsevier, p 259–V, https://doi.org/https://doi.org/10.1016/S0065-2687(02)80007-3, URL https://www.sciencedirect.com/science/article/pii/S0065268702800073

Wong TF (1982) Micromechanics of faulting in westerly granite. International Journal of Rock Mechanics and Mining Sciences & Geomechanics Abstracts 19(2):49–64. https://doi.org/https://doi.org/10.1016/0148-9062(82)91631-X, URL https://www.sciencedirect.com/science/article/pii/014890628291631X

Wu R, Selvadurai PA, Chen C, et al (2021) Revisiting Piezoelectric Sensor Calibration Methods Using Elastodynamic Body Waves. Journal of Nondestructive Evaluation 40(3):68. https://doi.org/10.1007/s10921-021-00799-1, URL https://doi.org/10.1007/s10921-021-00799-1

Yoshimitsu N, Kawakata H, Takahashi N (2014) Magnitude -7 level earthquakes: A new lower limit of self-similarity in seismic scaling relationships. Geophysical Research Letters 41(13):4495–4502. https://doi.org/https://doi.org/10.1002/2014GL060306, URL https://agupubs.onlinelibrary.wiley.com/doi/abs/10.1002/2014GL060306, https://agupubs.onlinelibrary.wiley.com/doi/pdf/10.1002/2014GL060306

Zhang S, Liu H, Cheng J, et al (2020) A mechanical model to interpret distributed fiber optic strain measurement at displacement discontinuities. Structural Health Mmonitoring 0(0):1475921720964183. https://doi.org/10.1177/1475921720964183, URL https://doi.org/10.1177/1475921720964183, https://doi.org/10.1177/1475921720964183